Planetary and Space Science 87 (2013) 1–13

Contents lists available at ScienceDirect

Planetary and Space Science

journal homepage: www.elsevier.com/locate/pss

# Highly accurate isotope composition measurements by a miniature laser ablation mass spectrometer designed for in situ investigations on planetary surfaces

A. Riedo [a,*], S. Meyer [a], B. Heredia [b], M.B. Neuland [a], A. Bieler [a], M. Tulej [a], I. Leya [a], M. Iakovleva [a], K. Mezger [b], P. Wurz [a]

[a] Space Research and Planetary Sciences, Physics Institute, University of Bern, Sidlerstrasse 5, 3012 Bern, Switzerland
[b] Institute of Geological Sciences, University of Bern, 3012 Bern, Switzerland

ARTICLE INFO

*Article history:*
Received 7 December 2012
Received in revised form
17 July 2013
Accepted 6 September 2013
Available online 25 September 2013

*Keywords:*
Accurate isotope measurement
Miniature laser ablation mass spectrometer
Space research
In situ measurement
Chemical analysis

ABSTRACT

An experimental procedure for precise and accurate measurements of isotope abundances by a miniature laser ablation mass spectrometer for space research is described. The measurements were conducted on different untreated NIST standards and galena samples by applying pulsed UV laser radiation (266 nm, 3 ns and 20 Hz) for ablation, atomisation, and ionisation of the sample material. Mass spectra of released ions are measured by a reflectron-type time-of-flight mass analyser. A computer controlled performance optimiser was used to operate the system at maximum ion transmission and mass resolution. At optimal experimental conditions, the best relative accuracy and precision achieved for Pb isotope compositions are at the per mill level and were obtained in a range of applied laser irradiances and a defined number of accumulated spectra. A similar relative accuracy and precision was achieved in the study of Pb isotope compositions in terrestrial galena samples. The results for the galena samples are similar to those obtained with a thermal ionisation mass spectrometer (TIMS). The studies of the isotope composition of other elements yielded relative accuracy and precision at the per mill level too, with characteristic instrument parameters for each element. The relative accuracy and precision of the measurements is degrading with lower element/isotope concentration in a sample. For the elements with abundances below 100 ppm these values drop to the percent level. Depending on the isotopic abundances of Pb in minerals, $^{207}Pb/^{206}Pb$ ages with accuracy in the range of tens of millions of years can be achieved.



## 1. Introduction

Determination of precise and accurate isotope compositions is of considerable importance in fundamental and applied research fields (Becker, 2007). In environmental research isotope analyses can provide a measure of element contamination in various solid materials and clarify the sources of these contaminants (Shotyk et al., 2005). Isotopes are helpful to study the distribution and transport of elements in plants (Becker and Dietze, 2000) and can be used to study element/isotope redistribution in biological samples (Lobinski et al., 2006) or single cell analysis in medical applications (Ng and Cheung, 2000; Zoriy et al., 2006). Isotope ratio measurements are used for fingerprinting of foods (Branch et al., 2003), to trace origins of plants and fruit, and for the quality control of agricultural products (Prohaska et al., 2003). Environmental monitoring, radioactive waste control and forensic investigations are other large fields where isotope ratios are used for diagnostic or searches of sources of material contamination (Ghazi and Millette, 2004; Becker, 2005).

The studies of isotope variations in solar system objects are of particular importance. The knowledge of the isotope composition and its variation in a given material may allow conclusions on the origin and evolution of our solar system. The studies of extraterrestrial materials provide insight into geochemical processes, constrain the time of formation of planetary material (crystallisation ages), and can be robust tracers of pre-solar events and processes (Tolstikhin and Kramers, 2008; Blichert-Toft et al., 2010; Bouvier and Wadhwa, 2010; McSween and Huss, 2010). Quantitative measurements of the elements and isotope ratios of planetary object matter can impose critical constraints on events and their chronology in the early stages of solar system formation. The data can also provide deeper insights into processes occurring on the surface of planetary bodies. With recent advances in dating of primitive meteoritic material, the evolution of early stages of the solar system could be well characterised (e.g., Russel et al., 2006; Blichert-Toft et al., 2010; Bouvier and Wadhwa, 2010). Absolute ages via the Pb–Pb dating technique offer the possibility of determining the crystallisation ages of rocks

* Corresponding author. Tel.: +41 31 631 44 49; fax: +41 31 631 44 05.
*E-mail address:* andreas.riedo@space.unibe.ch (A. Riedo).

0032-0633/$ - see front matter © 2013 Elsevier Ltd. All rights reserved.
http://dx.doi.org/10.1016/j.pss.2013.09.007

and minerals with an uncertainty of a few million years. Measurements of elemental and isotopic fractionation effects of other non-radiogenic elements are of interest too, because they yield information on the conditions and differentiation processes in the early solar system.

Development of space instrumentation, capable to conduct precise and accurate measurements of isotope ratios of material on planetary surfaces, is of interest to cosmochemistry and planetary sciences and drives present investigations. A detailed understanding of the chronology of the early solar system and dating of planetary materials require precise and accurate measurements of isotope ratios (e.g., Pb) and trace element abundances. However, such measurements are extremely challenging and until now, they have never been attempted in the space research. Gas phase analyses by space instruments such as Ptolemy on Rosetta should have the capability of achieving analytical precisions of about 5‰ or better and the Gas Analytical Package on Beagle 2 of about 1‰ or better for isotope ratios (Pullan et al., 2004; Todd et al., 2007; Wright et al., 2007; Gibson et al., 2010). Generally, present instrumentation for space research designed for investigations of the chemical composition of solid materials allow for the measurement of elements at concentrations down to the per mill level at best (McSween et al., 2011; Sinha et al., 2011). Instruments with improved detection limits are necessary, but so far, available only in the laboratory (Wurz et al., 2010; Riedo et al., 2013). Isotope compositions are usually measured with advanced mass spectrometric techniques. Among others, inductively coupled plasma mass spectrometry (ICP MS), thermal ionisation mass spectrometry (TIMS), secondary ion mass spectrometry (SIMS), spark source mass spectrometry (SSMS), laser ionisation mass spectrometry (LIMS) and resonance ionisation mass spectrometry (RIMS) are the most prominent methods (Becker, 2007). The first three methods are most often used in the present laboratory practice. They allow for sensitive, precise, and accurate measurements of isotope ratios of a variety of solid materials. Multi-collector ICP MS and TIMS instruments are currently perhaps the most widely used because of their high sensitivity and accuracy. Typically, TIMS offers very high measurement accuracy and precision, which are in general better than that of LA ICP MS. The disadvantage of TIMS measurements is that they are restricted to elements with an ionisation potential lower than 7 eV (Becker, 2002) and require chemically pure separation of the element of interest prior to the measurement. Nevertheless, these three techniques require extensive calibration measurements. LIMS is another sensitive mass spectrometric technique. So far, it is less commonly used for isotope measurements and it has been considered for some time as a semi-quantitative method in both element and isotope abundance determination (Becker and Dietze, 2000; Becker, 2002). LIMS has, however, still some potential for improvement. With recent progress in laser technology, fast electronics, and vacuum technology, this technique becomes attractive for chemical analysis of solid samples (Yu et al., 2009a; Lin et al., 2010; Tulej et al., 2011). Recent studies by Zhang et al. (2013) showed that at certain laser power densities matrix effects can be minimised and the best quantitative performance can be achieved by using a femtosecond laser ablation ion source.

In contrast to LA ICP MS or TIMS methods, LIMS offers simplicity of operation, no need for additional consumables (e.g., He for ICP MS), and robustness of the instrument construction. By combining a laser ion ablation source with time-of-flight mass spectrometer (TOF MS) full compositional analysis of solid material can be performed by consuming only picogram amounts of a sample (Yu et al., 2009b; Neuland et al., this issue). Due to progress in miniaturisation of the instrument initiated in 90 s and stimulated by spacecraft requirements, current LIMS instruments (LAZMA, LAMS and LMS) are well suited for in situ investigation of elemental composition (Managadze and Shutyaev, 1993; Brinckerhoff et al., 2000; Rohner et al., 2004; Managadze et al., 2010). Studies of the instrument performance showed that miniaturised LIMS systems can be highly sensitive in the detection of elements, reaching sub-ppm detection levels. Nevertheless, accuracy and precision of the measurements of the isotope composition of solids were determined usually with about 1% (Managadze et al., 2010; Tulej et al., 2011).

Here we report on the investigation of the capability of a miniaturised laser ablation instrument (LMS) developed for space research to measure precisely and accurately the isotope composition of Pb, used as a test case for the technique. The abundance of Pb-isotopes can be used for absolute radio-isotope chronology of planetary materials (e.g., the $^{207}$Pb–$^{206}$Pb dating method). In the following we describe a measuring procedure that was developed for obtaining highly reproducible spectra of Pb isotopes. A similar analytical procedure was applied for the investigations of other elements abundant in NIST standard reference materials (SRM), to find a correlation between relative measurement accuracy and precision and element/isotope concentration.

## 2. Experimental

### 2.1. Samples

For the investigations of Pb isotope compositions, untreated samples of the common Pb isotope standard from NIST, SRM 981, and three different galena samples (most abundant and widely distributed lead sulphide minerals) from different Pb ore mines, i.e., Kengere, Katagne, Democratic Republic of the Congo (Be 36), Dilia Mine, Kilo Moto, Democratic Republic of the Congo (Be 62), and Ambatofangehana, District Ambositra, Madagascar (Be 96), were used. The isotope composition of Pb in SRM 981 is given by the NIST certificate accompanying the reference material (Table 1). The isotope composition in the galena samples were measured by TIMS at the Institute of Geological Sciences at the University of Bern and taken as reference data to compare with LMS measurements (Section 2.2). To find a correlation between measurement accuracy and isotope concentration, the studies of isotope compositions of several other elements with different elemental/isotope concentration were performed using unprocessed NIST standard reference materials, including electrolytic iron, carbon iron, and steel (SRM 661, SRM 664, SRM 665). Because only elemental abundances are quoted by NIST for elements in these three reference materials, terrestrial isotope composition was assumed (Becker, 2007). All samples are homogeneous and the correlation studies, which required often several measuring campaigns, were performed always on the same sample material but at different sampling spots.

### 2.2. Measurements by thermal ionisation mass spectrometry (TIMS)

#### 2.2.1. Sample preparation

The galena samples were dissolved in 6 N HCl and loaded on a single Rhenium filaments using a silica-gel/$H_3PO_4$ acid mixture (Gerstenberger and Haase, 1997).

**Table 1**
Isotopic composition (in atomic fraction) of Pb in SRM 981 as quoted by NIST. Quoted errors correspond to the 95% confidence interval.

| Mass [amu] | Isotopic composition [at%] |
|---|---|
| $^{204}$Pb | $1.4255 \pm 0.0012$ |
| $^{206}$Pb | $24.1442 \pm 0.0057$ |
| $^{207}$Pb | $22.0833 \pm 0.0027$ |
| $^{208}$Pb | $52.3470 \pm 0.0086$ |

**Table 2**
Isotope composition of Pb measured in galena samples Be 36, Be 62 and Be 96, measured with TIMS (uncertainties based on individual run statistics).

| Galena sample | Mass [m/q] | Isotope composition [at%] |
|---|---|---|
| **Be 36** | 204 | $1.38010 \pm 0.00065$ |
| | 206 | $24.858 \pm 0.016$ |
| | 207 | $21.609 \pm 0.017$ |
| | 208 | $52.153 \pm 0.050$ |
| **Be 62** | 204 | $1.48680 \pm 0.00069$ |
| | 206 | $23.205 \pm 0.014$ |
| | 207 | $22.801 \pm 0.018$ |
| | 208 | $52.508 \pm 0.049$ |
| **Be 96** | 204 | $1.41347 \pm 0.00066$ |
| | 206 | $24.479 \pm 0.016$ |
| | 207 | $22.219 \pm 0.018$ |
| | 208 | $51.888 \pm 0.049$ |

### 2.2.2. Setup and measurements

Isotope ratios were measured using a $Pb^+$ beam on a Thermo Fischer Triton$^+$ multi-collector thermal ionisation mass spectrometer in static Faraday mode. During the course of the analysis a signal intensity of 1–4 V for mass $^{206}Pb$ was maintained. The mean of the Pb-isotope ratios for the galena samples is based on 75 scans. The raw isotope ratios were corrected for mass fractionation with a factor of $0.14 \pm 0.02\%/amu \pm 1\sigma$ (abs) based on multiple analyses of the standard NBS SRM 981 and SRM 982. At the time of the measurements, the reproducibility of the standard NBS SRM 982 was 0.05%, 0.03% and 0.09% for the $^{206}Pb/^{204}Pb$, $^{207}Pb/^{204}Pb$, and $^{208}Pb/^{204}Pb$ ratios, respectively. The total procedural blank of $< 10$ pg Pb is negligible. Table 2 shows the measurement results of the isotopic composition of Pb in the three different galena samples analysed.

### 2.3. Measurements by laser ionisation mass spectrometry using LMS instrument

Only a brief introduction of the experimental setup and the principles of the operation of LMS are given here. A more detailed description can be found in previous publications (Rohner et al., 2003; Tulej et al., 2011, 2012; Riedo et al., 2013). A discussion about a flight version of the present LMS instrument can be found in Riedo et al. (2013).

The experimental system consists of a laser ablation ion source and a miniature reflectron-time-of-flight mass spectrometer (Figs. 1 and 2). The dimensions of the mass spectrometer are 160 mm × ⌀60 mm. The instrument and the solid samples are placed within an UHV chamber (Fig. 2), which has a typical base pressure in the low $10^{-8}$ mbar range. A Q-switched frequency quadrupled Nd:YAG laser system (266 nm, $\tau \approx 3$ ns, repetition rate of 20 Hz) is used to ablate surface material. The laser output is controlled by a tuneable polarisation-sensitive attenuator to adjust the laser fluences. The laser beam is focused to a spot size with a diameter of 20 μm on the sample surface. The laser beam is guided with mirrors and is co-linear with the principle ion-optical axis of the LMS system. The laser beam then enters the mass analyser through a window at the top of the vacuum chamber and a focusing lens. The focused laser beam passes through the mass analyser, the detection assembly with a central hole of ⌀6.4 mm, and the ion optical system, all the way down until it reaches the sample surface (Figs. 1 and 2).

Positive ions from the plasma plume enter the mass analyser through a conical nose-piece, and are accelerated, confined, and collimated by an electrostatic immersion lens. Four electric potentials accelerate and focus the ions into the field-free and reflectron regions from which ions are reflected and detected by a pair of multichannel plates (MCP) used in a chevron configuration. An initial voltage set for the ion optical system was determined from ion optical simulations (Rohner et al., 2003). These values are taken as a start set of voltages for the further voltage optimisation procedure controlled by a dedicated and self-written code (Bieler et al., 2011; Bieler, 2012; Riedo et al., 2013). The signals generated in the MCP are collected by four concentric anode rings. Ions of

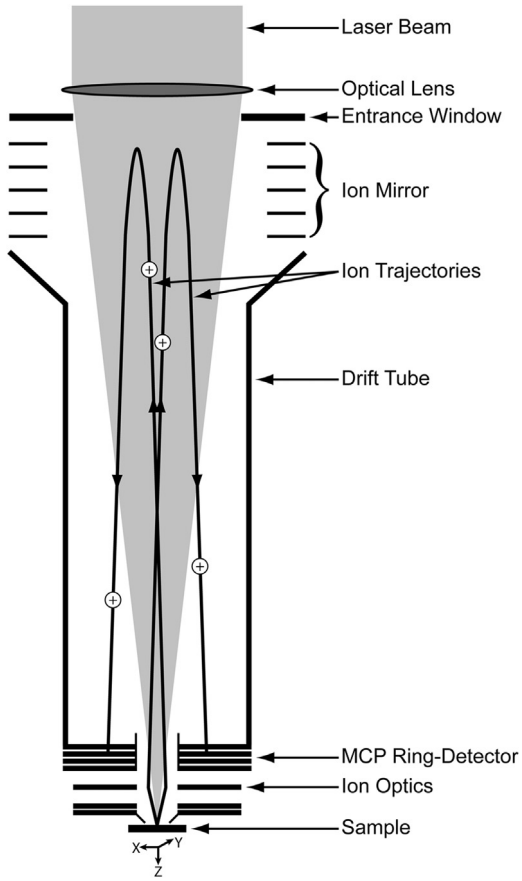


**Fig. 1.** Schematic overview of the set-up and operation principles of a laser ablation mass analyser. A wide circular laser beam (~⌀30 mm) enters the mass analyser from the top and is focused by an optical lens (f/200, NA=4) onto the sample surface after travelling through the interior of the mass analyser. The ions generated during the ablation process are accelerated, confined, and collimated by the ion optics, reflected by an ion mirror, and detected by the MCP ring-detector.

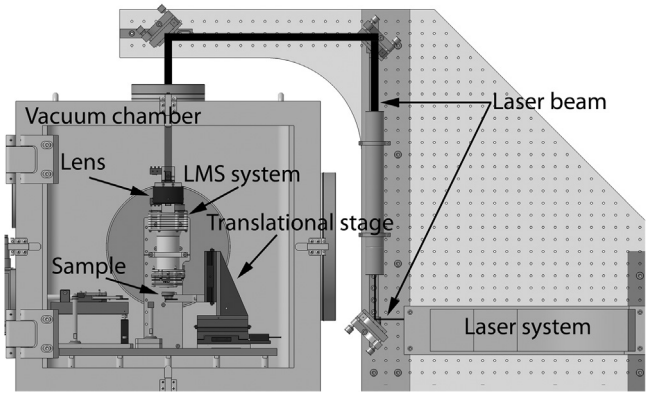


**Fig. 2.** Engineering drawing of the experimental setup. A UV laser beam from a Nd:YAG laser is guided with dielectric mirrors to the top of the vacuum chamber. A miniature mass analyser is placed in a vacuum chamber. The sample is placed just in the front of the mass analyser on a sample holder positioned by *x*, *y*, *z* micro-translational stages (Riedo et al., 2013).

different mass arrive at the MCP detector in sequence, at times proportional to the square root of their mass-to-charge ratio (m/q).

Samples are placed on a sample holder mounted on the *x*, *y*, *z* micro-translational stages (Fig. 2) and are positioned at a fixed distance, typically ~1 mm, from the grounded entrance plate of the mass spectrometer.

The pulsed laser system initiates the experimental cycle and triggers the data acquisition. For this study time-of-flight spectra from one of the four anode rings of the MCP detector are recorded with one channel of a dual-channel, 8-bit PCIe high-speed digitizer ADC card with on-board signal processing (Agilent, U1084A). In single-channel mode, this card supports 4 GS $s^{-1}$ with an analogue bandwidth of 1.5 GHz. The spectra are recorded typically in the mass/charge range of 0–250 m/q, corresponding to flight times up to ~15 μs (Riedo et al., 2013). A dynamic measurement range of at least 8 orders of magnitude can be achieved by recording time-of-flight spectra from two additional anode rings simultaneously with one additional dual-channel ADC card. In this case the spectra are recorded at different ADC gain levels to measure high intensity signals (elements and isotopes with abundances down to ~100 ppm, weight fraction) and signals just above the instrumental noise (isotopes with abundances in the ppb range, weight fraction) simultaneously. More information about this measurement procedure can be found in (Riedo et al., 2013).

### 2.3.1. Optimisation of measuring procedure

The choice of voltage settings for the ion optics and the control of laser ablation conditions including laser fluence and laser irradiance levels, laser focusing geometry, and distance between sample and entrance of the instrument are the crucial parameters for quantitative measurements with a high spatial resolution. Before starting experimental campaigns, the instrument performance is optimised using the procedure described previously (Bieler et al., 2011; Bieler, 2012; Riedo et al., 2013). This procedure optimises a function of the ion transmission and mass resolution yielding a mass resolution typically in the range of $m/\Delta m = 500–700$ for the $^{56}Fe$ mass peak.

The sample is positioned typically about ~1 mm away from the entrance plate, which corresponds roughly to the focal point of the laser. The optimisation procedure described previously (Bieler et al., 2011; Bieler, 2012; Riedo et al., 2013) is used to optimise the voltages of the ion-optical system. Communication with the high-voltage power supply for the instrument is made via a RS232 interface. The settings of the acquisition card allow measurements of the mass peak selected for optimisation.

The optimisation code is based on an adaptive particle swarm algorithm (Bieler et al., 2011; Bieler, 2012) and is used to tune the ion-optical system by adjusting the voltage settings after the analysis of the mass peak to optimise the ion transmission and mass resolution. This adjustment minimises a user defined fitness-function, e.g., *–A/FWHM*, where *A* and *FWHM* denote the amplitude and the full-width at half maximum of a user selected peak for optimisation. If the desired mass resolution $m/\Delta m$ and ion transmission are not achieved with the first optimisation procedure the laser fluence and the sample distance to the mass analyser entrance can be adjusted.

### 2.3.2. Measurement procedure

Each of the measurements discussed here were performed on a new and untreated spot on the sample surface. In the following, the measurement procedure for highly accurate measurements is discussed:

i) *Optimisation of the mass resolution and ion transmission of the instrument.*
   The operational instrument mass resolution was typically within the range of $m/\Delta m \sim 500–700$ allowing well separation of isotope peaks from each other. High ion transmission is also obtained by the optimisation process. The dynamic range of the instrument is about 8 orders of magnitude allowing for the detection of elements present at sub-ppm levels (Riedo et al., 2013). The signal-to-noise ratio (SNR) is defined as the ratio of the maximum amplitude of the analysed peak divided by the standard deviation of noise within a range of 1 m/q, analysed in an area of the spectrum where no mass peaks are detected.
ii) *Choice of the number of single laser shot spectra for final mass spectrum.*
   A final mass spectrum is the result of a relatively high number of averaged measurements, typically consisting of several 10,000 single laser shot spectra, which are collected from one sample location. For most analyses, a sequence of spectra of an intermediate number of accumulations, typically histograms of 100 single shot spectra, are saved on the host computer, and later added to the final spectrum corresponding to several 10,000 single shot spectra. This sequence is used to study the dependence of the cumulative sum of the integrated peak areas, the SNR, the mass resolution $m/\Delta m$, and the relative measurement accuracy on the number of accumulated spectra. Furthermore, the number of accumulated spectra needed is correlated to the isotope abundance in the sample and the instrumental detection sensitivity of the investigated element (Tulej et al., 2012; Riedo et al., 2013).
iii) *Choice of applied laser irradiance.*
   Several measurement campaigns, each consisting of the defined number of accumulated spectra, have to be conducted at different laser fluences to find the best relative measurement accuracy.

### 2.3.3. Case study Pb—SRM 981 and galena samples

A measurement campaign on a Pb sample of SRM 981 (Pb metal) was conducted by ablating the surface continuously with 100,000 laser shots at a laser irradiance of ~0.3 GW/$cm^2$. Histograms of 100 single laser shot spectra were sequentially saved on the host computer (1000 histograms in total). SNR, mass resolution, measurement accuracy, and cumulative sum of the integrated peak areas were histogramed and analysed for spectra accumulations of 1000, 5000, 10,000, 20,000, …, 100,000. The resulting analysis shows that to conduct a quantitative measurement of an isotope composition with a precision at the per mill level, the spectra obtained from the ablation of the first 20,000 laser shots are optimal. In the following, 11 measurements parameterised by laser irradiances (tuning of the laser fluence) in the range of about 0.1–0.6 GW/$cm^2$ were finally conducted. The studies of the galena samples were performed by employing the same accumulation of spectra, and by applying the laser irradiances in the range that yielded the most accurate measurements for the SRM 981 sample. On each of the three galena samples several campaigns parameterised by laser irradiances were performed to establish the reproducibility of the results and possible dependences on sample surface morphology and composition.

### 2.3.4. Study of isotope composition of selected elements

Several measurement campaigns on different NIST standards (SRM 661, 664, 665, and 981) were performed to study the correlation between elemental/isotope abundance and relative measurement accuracies. In case of SRM 661, 664, and 665 elemental concentrations are given by NIST in weight fractions. The isotope abundances were calculated by assuming terrestrial isotope ratios (Becker, 2007). For laser ablation mass spectrometry NIST quoted elemental concentrations in weight fractions were converted into elemental concentrations in atomic fractions (Tulej et al., 2011), and again, isotope abundances were calculated by assuming terrestrial isotope ratios (Becker, 2007). Depending on the elemental/isotope abundance in the investigated sample and detection sensitivity for

**Table 3**
Elemental abundances in weight fractions for different metallic and non-metallic elements as given by NIST for SRM 665, 664, and 661 (second column). Isotope abundances (in weight fractions [ppm], third column) were calculated assuming terrestrial isotope ratios (Becker, 2007). Elemental and isotope abundances calculated for laser ablation mass spectrometry are given in atomic fractions [ppm] in fourth and fifth column. SRM 981 is a Pb isotope standard sample; isotope ratios in atom fractions as given by NIST (see also Table 1).

| Element | Weight fraction element [ppm] | Weight fraction isotope [ppm] | Atom fraction element [ppm] | Atom fraction isotope [ppm] |
|---|---|---|---|---|
| B (SRM 665) | 1.3 | $^{10}$B: 0.26<br>$^{11}$B: 1.04 | 6.7 | $^{10}$B: 1.34<br>$^{11}$B: 5.37 |
| C (SRM 665) | 80.0 | $^{12}$C: 79.14<br>$^{13}$C: 0.86 | 371.6 | $^{12}$C: 367.61<br>$^{13}$C: 3.98 |
| S (SRM 665) | 59.0 | $^{32}$S: 56.04<br>$^{34}$S: 2.51 | 102.7 | $^{32}$S: 97.51<br>$^{34}$S: 4.36 |
| Ti (SRM 665) | 6.0 | $^{46}$Ti: 0.50<br>$^{48}$Ti: 4.42<br>$^{49}$Ti: 0.32 | 7.0 | $^{46}$Ti: 0.58<br>$^{48}$Ti: 5.16<br>$^{49}$Ti: 0.38 |
| Ti (SRM 664) | 2300.0 | $^{46}$Ti: 189.75<br>$^{47}$Ti: 171.12<br>$^{48}$Ti: 1695.56<br>$^{49}$Ti: 124.22 | 2610.3 | $^{46}$Ti: 215.35<br>$^{47}$Ti: 194.21<br>$^{48}$Ti: 1924.31<br>$^{49}$Ti: 140.98 |
| Cr (SRM 661) | 6900.0 | $^{52}$Cr: 5781.44<br>$^{53}$Cr: 655.57 | 7294.9 | $^{52}$Cr: 6112.29<br>$^{53}$Cr: 693.08 |
| Zr (SRM 664) | 690.0 | $^{90}$Zr: 355.01<br>$^{91}$Zr: 77.42 | 410.9 | $^{90}$Zr: 211.41<br>$^{91}$Zr: 46.10 |
| Pb (SRM 981) | – | – | 1,000,000 | $^{204}$Pb: 14,255<br>$^{206}$Pb: 241,442<br>$^{207}$Pb: 220,833<br>$^{208}$Pb: 523,470 |

the isotopes, campaigns of up to 40,000 accumulated/averaged spectra were conducted. Table 3 gives an overview of the investigated elements/isotopes and their abundances.

### 2.3.5. Data analysis

Curve fitting functions, such as Gaussian (Eq. (1)), Exponentially Modified Gaussian (EMG, Eq. (2)), etc., are typically used for simplicity to fit and analyse experimental mass peaks. These methods of least squares, however, consistently underestimate the area under a fitted curve (Bevington and Robinson, 2003). For this reason, two curve fitting functions, Gaussian (Eq. (1)) and EMG (Eq. (2)), and two direct integration methods, spline interpolation and Monte-Carlo integration, were used for the data analysis. For both direct integration methods, the integration window was set manually, typically in the turn-over between two mass peaks. The subsequent results are compared to the reference.

*Gaussian – fit function* :

$$f_{Gaussian}(x) = \frac{A}{\sigma\sqrt{2\pi}} e^{-1/2(x-\mu/\sigma)^2}, \quad (1)$$

where $A$ denotes the peak area, $\mu$ the centre and $\sigma$ correlates to the full width at half maximum (FWHM) of the analysed peak.

*EMG – fit function* :

$$f_{EMG}(x) = \frac{A}{2\tau} e^{\left(\frac{\sigma^2}{2\tau^2} - \left(\frac{x-\mu}{\tau}\right)\right)} \left[1 + erf\left(\frac{1}{\sqrt{2}}\left(\frac{x-\mu}{\sigma} - \frac{\sigma}{\tau}\right)\right)\right],$$
$$erf(\alpha) = \frac{2}{\sqrt{\pi}} \int_0^{\alpha} e^{-y^2} dy, \quad (2)$$

where $A$ describes the peak area, $\mu$ the weighted centre of the peak (no longer the maximum point), $\sigma$ denotes the half width of the Gaussian part, $\tau$ the exponentially decay of the function, and $erf(\alpha)$ is the error function.

A comparison between the Gaussian- and the EMG-fit function is shown in Fig. 3.

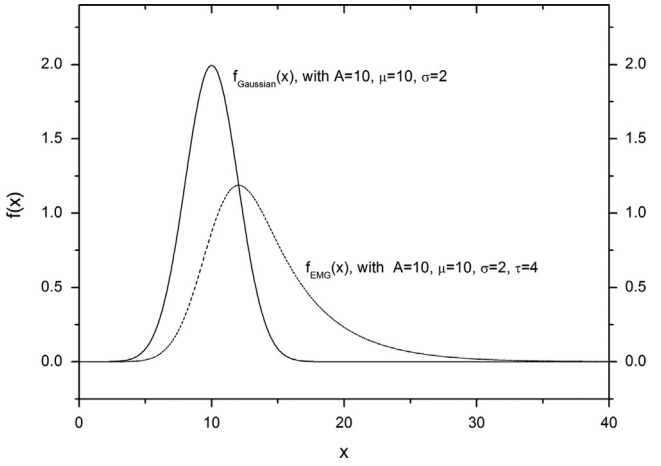


**Fig. 3.** Comparison between the Gaussian- and the EMG- (Exponentially Modified Gaussian) fit functions. The EMG introduces asymmetry to the Gaussian shaped curve, which commonly models the shape of the experimental mass peak well.

*Spline direct integration:*

We used a cubic spline interpolation with an adaptive Simpson quadrature integration. This allows very fast integration (a few seconds of CPU computing time of Desktop PC) of the mass peaks with a shape interpolated by spline functions. Unfortunately, the uncertainties introduced by this method are unknown because the Simpson quadrature integration error is of the order four, exactly the same as for cubic polynomials. The lack of an error estimate is the main disadvantage of this method, compared to other analysis methods.

*Monte-Carlo direct integration:*

The Monte-Carlo integration method uses uniformly distributed random numbers in a defined mass versus intensity array chosen for the integration to generate virtual data points. The virtual data points are distributed over the sampling grid of the defined array. Each virtual data point was compared with the measured data at defined grid position and either accepted, if is found inside the measured

data, or rejected, if not. The area of the measured mass peak is then equal to the fraction of accepted to the total generated virtual data points times the area of the defined window (Fig. 4). The main disadvantage of this method is the calculation time, which increases dramatically with the number of repetitions and the number of virtual data points, e.g. about 10 min for a $100 \times 10^6$ integration of one mass peak. The accuracy of this method is limited by the sample width of the measurement data. Further information about the Monte-Carlo integration method can be found in Bevington and Robinson (2003). The number of repetitions and virtual data points were evaluated by using a known test signal. For evaluation of the uncertainty of the analysis, the method was repeated $n=100$ times with $10^6$–$10^7$ virtual data points.

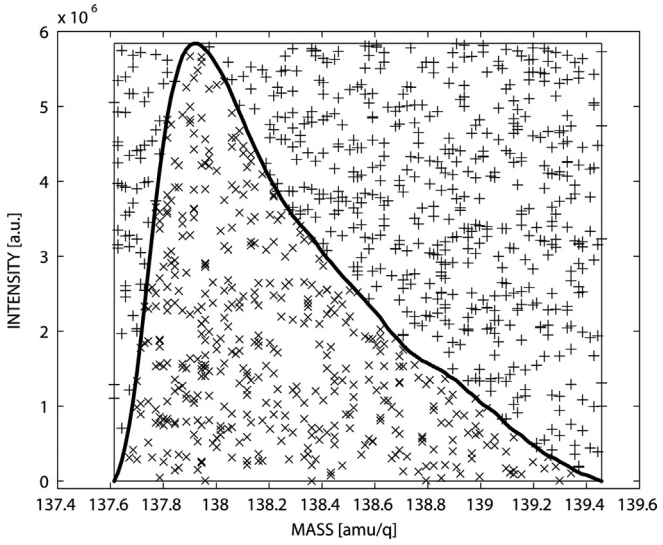


**Fig. 4.** The schematic principle of the acceptance ($x$) and the rejection ($+$) method of randomly generated data points within the defined window for a $^{138}$Ba-peak measured in galena sample Be 96 of the Monte-Carlo simulation is shown.

## 3. Results and discussion

### 3.1. Case study Pb—NIST SRM 981

#### 3.1.1. Study on the number of accumulated spectra

The dependence of the measurement parameters on the number of accumulated spectra are shown in Fig. 5 for $^{204}$Pb, $^{206}$Pb, $^{207}$Pb and $^{208}$Pb in SRM 981, which are the isotopic peak areas (panel a), SNR (panel b), mass resolution $m/\Delta m$ (panel c), and relative measurement accuracies (panel d) defined as |NIST abundance-measured abundance|/NIST abundance. The campaign was performed at one sample location on SRM 981 by applying a laser irradiance of $\sim$0.3 GW/cm$^2$ and consists in total of 100,000 single laser shot spectra (1000 histograms each being a spectrum of 100 single shot averages). The measurement parameters are determined and analysed after accumulation of 1000, 5000, 10,000, 20,000, …, 100,000 single shot spectra. The isotope peak areas and relative measurement accuracies were analysed by using the Monte-Carlo integration ($n=100$ repetitions with $10^6$ data points each) and the Gaussian-fit model is used to calculate the mass resolution.

The increase of the accumulated isotope peak area (panel a) with increasing number of accumulated spectra is as expected. The SNR (panel b) rises with number of accumulated spectra, as

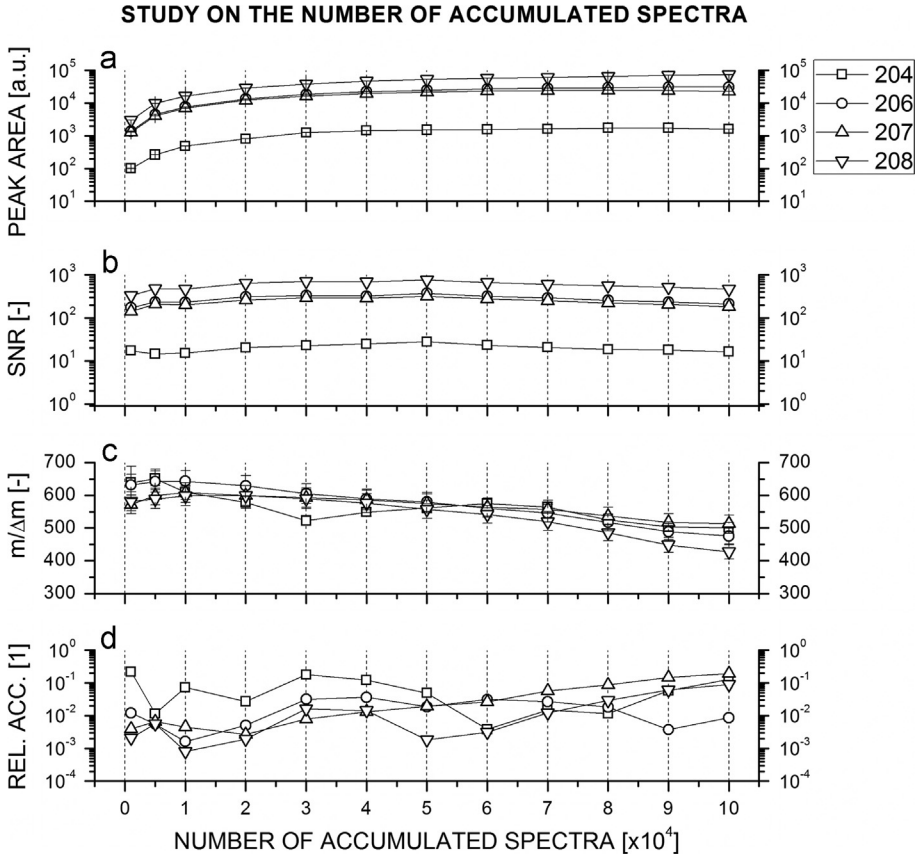


**Fig. 5.** Analysis of the Pb isotopes $^{204}$Pb, $^{206}$Pb, $^{207}$Pb, and $^{208}$Pb in NIST SRM 981 sample. The measurement parameters *peak area*, *SNR*, *mass resolution* $m/\Delta m$, and the *relative measurement accuracy* are shown as a function of the number of accumulated spectra.

expected from the statistical improvement, until the accumulation of about 20,000 spectra. In the first 20,000 accumulated spectra, the mass resolution remains approximately constant at $m/\Delta m \sim$ 600–700. For further accumulations the mass resolution steadily decreases, reducing the SNR. With increase of aspect ratio of the ablation crater (depth/diameter) with increase of number of laser shots the conditions of laser ablation ion source are expected to change significantly. At increased number of laser shots the ablation crater changes its form from "flat-bottom" to a "cone-shape", which can be one of the reasons of downgrading the focusing capability of the ion optical system as observed in Russo et al. (2002). Taking these observations into account, we find that the best measurement performance, including the measurements of isotope compositions with relative measurement accuracies at the level of per mill (panel d), are obtained by analysis of the first 20,000 accumulations of single shot spectra. A decrease of relative accuracy to the percent level is observed for acquisitions of more than 20,000 individual single spectra.

### 3.1.2. Influence of laser irradiance

To establish the dependence of the relative measurement accuracies of the isotope composition on laser irradiance, the mass spectrometric measurements were conducted for 11 different laser irradiances in the range of 0.1–0.6 GW/cm$^2$, using each time a fresh sample surface. The spectra were obtained by accumulation of 20,000 single laser shot spectra. Fig. 6 summarises the results of these studies, where dependences of several parameters including the integrated isotopic peak area (panel a), SNR (panel b), mass resolution $m/\Delta m$ (panel c), and the relative measurement accuracy (panel d) on the laser irradiances are displayed. Overall, we observe an increase of the detection efficiency and an increase of the SNR with increasing laser irradiances (panel a and b, Fig. 6). Increase of the laser fluence causes an increase of the ablation rate and plasma plume temperature, which increases the number of ions in the gas phase and also the ionisation efficiencies. A decrease of the mass resolution $m/\Delta m$ (panel c) with an increase of laser irradiance is also observed as expected. Space charge effects, e.g., surface charging and Coulomb repulsion in the ion-optical system, become significant at higher laser fluences (irradiances) due to increased ion densities. These effects can broaden the ion distribution spatially and thereby cause deterioration of the mass resolution of the instrument. We find a plateau defining highest relative accuracies of the measurement within a laser irradiance range of 0.25–0.45 GW/cm$^2$ (panel d of Fig. 6), where accuracies at the level of ‰ are achieved for isotope ratios.

### 3.1.3. Numerical methods and their accuracies

In the following, the results from the application of various numerical methods for the analysis of the mass spectra are discussed. The classical peak fit methods using Gaussian- and EMG-fit functions, and two direct integration methods, Spline and Monte-Carlo integration, were used to integrate the peak areas and to obtain isotope abundance ratios for $^{204}$Pb, $^{206}$Pb, $^{207}$Pb, and $^{208}$Pb. The results of this analysis are compared with NIST reference values (see Tables 1, 4–7). In each table, the calculated isotopic ratios with their absolute accuracies in [%], defined as |quoted values − measured values|, and their relative accuracies in [‰], defined as |quoted values − measured values|/quoted values, are given. The errors correspond to $1-\sigma$ uncertainties. Fig. 7 shows the summary of all isotope abundance results that are listed in Tables 4–7. For comparison with NIST standards (Table 1) the displayed errors were recalculated to match the 95% confidence interval ($1.96 \times 1-\sigma$ errors given in Tables 4–7).

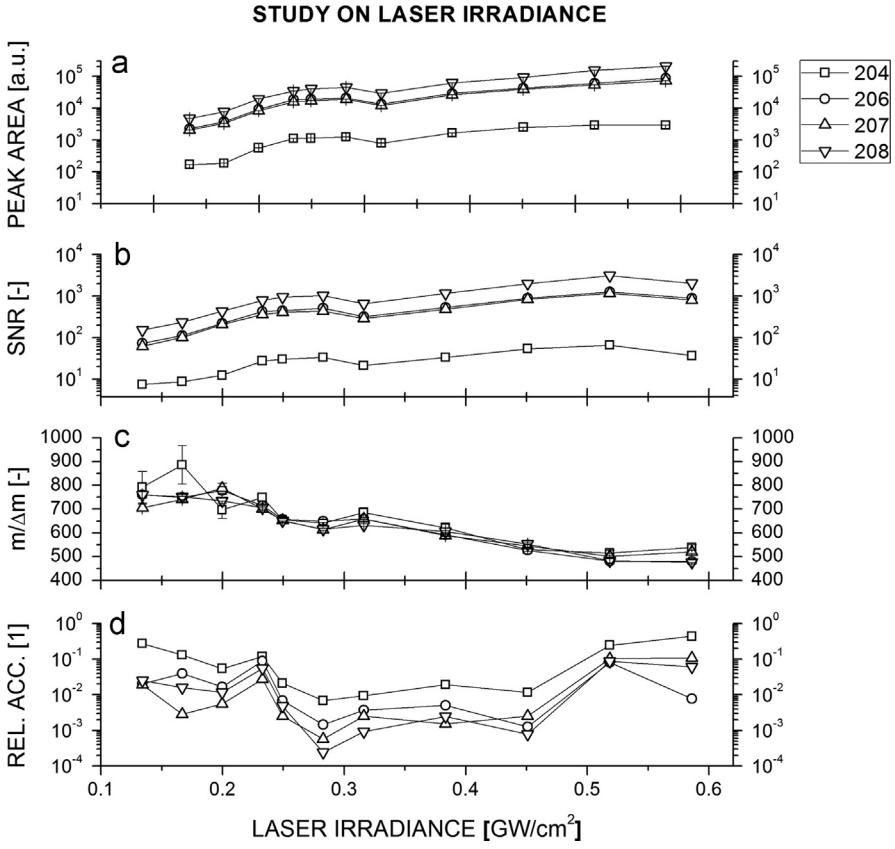


**Fig. 6.** Analysis of the $^{204}$Pb, $^{206}$Pb, $^{207}$Pb, and $^{208}$Pb in NIST SRM 981 sample. The dependence of mass peak area, SNR, mass resolution m/Δm, and the relative measurement accuracy on the laser irradiance is shown. Each data point is derived from the spectrum obtained by accumulation of 20,000 single laser shot spectra.

**Table 4**
Measured isotopic composition of Pb in SRM 981. The Gaussian-fit function is used to analyse the data. Errors are $1-\sigma$ values.

| Mass [m/q] | Isotope abundance [%] | Abs. accuracy [%] | Rel. accuracy [‰] |
|---|---|---|---|
| 204 | $1.559 \pm 0.031$ | $0.134 \pm 0.031$ | $93.7 \pm 21.8$ |
| 206 | $24.35 \pm 0.27$ | $0.21 \pm 0.27$ | $8.7 \pm 10.6$ |
| 207 | $22.26 \pm 0.17$ | $0.18 \pm 0.17$ | $8.2 \pm 7.7$ |
| 208 | $51.82 \pm 0.41$ | $0.52 \pm 0.41$ | $10.0 \pm 7.7$ |

**Table 5**
Measured isotopic composition of Pb in SRM 981. The EMG-fit function is used to analyse the data. Errors are $1-\sigma$ values.

| Mass [m/q] | Isotope abundance [%] | Abs. accuracy [%] | Rel. accuracy [‰] |
|---|---|---|---|
| 204 | $1.552 \pm 0.031$ | $0.127 \pm 0.031$ | $89.0 \pm 22.0$ |
| 206 | $24.34 \pm 0.19$ | $0.20 \pm 0.19$ | $8.2 \pm 7.9$ |
| 207 | $22.18 \pm 0.12$ | $0.09 \pm 0.12$ | $4.2 \pm 5.6$ |
| 208 | $51.93 \pm 0.17$ | $0.42 \pm 0.17$ | $8.0 \pm 3.2$ |

**Table 6**
Measured isotopic composition of Pb in SRM 981. The spline-interpolation function is used to analyse the data. Spline integration does not give an error estimate.

| Mass [m/q] | Isotope abundance [%] | Abs. accuracy [%] | Rel. accuracy [‰] |
|---|---|---|---|
| 204 | 1.4371 | 0.0116 | 8.1 |
| 206 | 24.1239 | 0.0203 | 0.8 |
| 207 | 22.1112 | 0.0279 | 1.3 |
| 208 | 52.3277 | 0.0193 | 0.4 |

**Table 7**
Measured isotopic composition of Pb in SRM 981. The MC function ($n=100$ repetitions with $10^7$ data points each) is used to analysis the data. Errors are $1-\sigma$ values.

| Mass [m/q] | Isotope abundance [%] | Abs. accuracy [%] | Rel. accuracy [‰] |
|---|---|---|---|
| 204 | $1.4364 \pm 0.0012$ | $0.0109 \pm 0.0012$ | $7.6 \pm 0.8$ |
| 206 | $24.122 \pm 0.010$ | $0.022 \pm 0.010$ | $0.9 \pm 0.4$ |
| 207 | $22.1105 \pm 0.0092$ | $0.0272 \pm 0.0092$ | $1.2 \pm 0.4$ |
| 208 | $52.331 \pm 0.029$ | $0.016 \pm 0.029$ | $0.3 \pm 0.6$ |

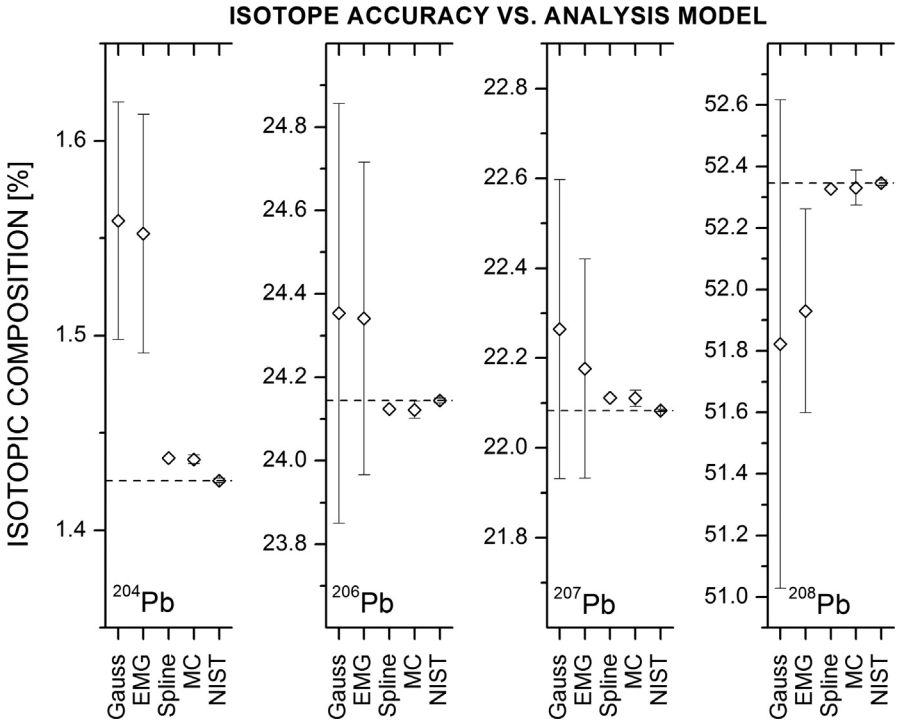


**Fig. 7.** Lead isotope composition in NIST SRM 981 determined by the Gaussian- and EMG-fit, and using Spline and Monte Carlo (MC) direct integration methods. The dashed lines correspond to NIST certified values. Errors give the 95% confidence level.

Fig. 7 displays the results obtained by the different analytical methods (data from Tables 4–7). Significantly larger systematic errors can be observed for the curve fitting methods, Gaussian- and EMG-fit functions, because the mass peak shape is not modelled perfectly by these methods. The increase of the systematic errors of the fitting methods (Fig. 7) is in agreement with the theoretical calculations discussed in Bevington and Robinson (2003). The method of least squares consistently underestimates the area under a fitted curve, which can be clearly observed in Fig. 7. The peak area of the major isotope $^{208}$Pb is underestimated, and hence, the isotope abundances of the other three less abundant Pb isotopes are enhanced relative to the certified values. The strongest effect can be observed for $^{204}$Pb due to its lowest isotope abundance. In comparison to the fitting methods the methods of direct integration (Spline and MC) show significant better agreement with the NIST certified values. Their relative accuracies of measurements are at the level of per mill and better (Tables 4–7).

### 3.2. Analysis of galena samples

The measurement results of the galena samples (Be 36, Be 62, and Be 96) are shown in Table 8. The isotopic compositions were calculated by using the MC direct integration method and compared to the TIMS measurements (see Table 2). By applying a similar measuring procedure as used for measurements of SRM 981 and the MC integration method, the relative measurement accuracies were determined to be at the per mill level (fourth column, Table 8). In Fig. 8 the comparison between TIMS and LMS measurements (Tables 2 and 8) is shown.

### 3.3. NIST study: isotope abundance versus measurement accuracy

Fig. 9 shows the correlation between isotope abundances and their relative measurement accuracies. The displayed error corresponds to the 95% confidence interval. A clear correlation between isotope abundance and relative measurement accuracies can be observed. Best accuracies, at the level of per mill and better, are observed at the highest abundances, as expected. At abundances of 10 ppm and lower accuracies degrade to tens of percent.

With the measured correlation between isotope abundances and accuracies (Fig. 9) we can derive an estimate for the uncertainty of the radio-isotope chronology using the $^{207}$Pb–$^{206}$Pb system. The estimate is based on a data set of $^{207}$Pb/$^{206}$Pb ages obtained from monazite grains in the sample 449105 investigated by Willigers et al. (2002) by laser ablation multiple-collector ICP-MS. The mean $^{207}$Pb/$^{206}$Pb age of monazite was measured as $1836 \pm 3$ Myrs (Willigers et al., 2002). In Table 9 data of the investigated grains (first column), $^{206}$Pb and $^{207}$Pb isotopic abundances (second and third column), $^{207}$Pb/$^{206}$Pb ratios, and ages (fourth and fifth column) of six different grains investigated in sample 449105 are listed (Willigers et al., 2002). In the sixth column the maximal $^{207}$Pb/$^{206}$Pb uncertainties estimated for an LMS measurement (Fig. 9) are given. The corresponding accuracies for the age determination, calculated as ($^{207}$Pb/$^{206}$Pb$_{age}$–($^{207}$Pb/$^{206}$Pb $\pm$ uncertainty)$_{age}$), are shown in the last column of Table 9. Including the error propagation of these six measurements (which is $(1/N)\sqrt{\sum_i accuracy_i^2}$, where $N$ denotes the number of measurements) a statistical uncertainty for the age determination by LMS of only about $\pm 26$ million years is derived for the combination of these measurements.

Fig. 10 shows the correlation between the abundance of $^{206}$Pb and $^{207}$Pb and the accuracy of the age determination by assuming a constant ratio of 0.11261 for $^{207}$Pb/$^{206}$Pb (Sample 449105, Grain A, Table 9). Filled squares are estimates if only a single measurement of one grain is considered. Open diamonds are estimates if 10 measurements are taken into account, which corresponds to a reduction of the uncertainty of about a factor of 3. In this case it should be possible to determine $^{207}$Pb/$^{206}$Pb ages with an accuracy of $\sim \pm 100$ Myrs using grains with $^{206}$Pb and $^{207}$Pb abundances in the range of $\sim$20 ppm and 2 ppm, respectively. Note that in both cases, decreasing the abundance of $^{206}$Pb while taking $^{207}$Pb/$^{206}$Pb ratio constant at 0.11261, the limiting factor for the final age is the uncertainty of $^{207}$Pb. This is because of the lower abundance of $^{207}$Pb. Its uncertainty is about a factor of 3 higher than the uncertainty for $^{206}$Pb.

SIMS U-Pb campaigns on several zircon grains from Apollo 14 and 17 breccias were conducted by Nemchin et al. (2008) to study the evolution of lunar KREEP. Many of the investigated zircons have $^{206}$Pb and $^{207}$Pb abundances in range of tens to hundreds of ppm. In the context of a lunar lander mission, the LMS instrument would be an ideal analysis tool for accurate in situ Pb–Pb dating of lunar materials. In comparison with other miniaturised instruments designed for in situ geochronology, e.g., the potassium–argon laser experiment (KARLE) instrument (Cohen, 2012), the design and measurement principle is robust and simple.

**Table 8**
Measured isotope abundances of Pb in the galena samples Be 36, Be 62 and Be 96 by using MC integrations of $n=100$ repetitions with $10^7$ data points each. TIMS measurements were taken as reference values (Table 2).

| Mass [m/q] | Isotopic abundance [%] | Abs. accuracy [%] | Rel. accuracy [‰] |
|---|---|---|---|
| **Be 36** | | | |
| 204 | $1.37675 \pm 0.00057$ | $0.00335 \pm 0.00057$ | $2.4 \pm 0.6$ |
| 206 | $24.965 \pm 0.011$ | $0.107 \pm 0.011$ | $4.3 \pm 0.8$ |
| 207 | $21.568 \pm 0.010$ | $0.041 \pm 0.010$ | $1.9 \pm 0.9$ |
| 208 | $52.090 \pm 0.027$ | $0.063 \pm 0.027$ | $1.2 \pm 1.1$ |
| **Be 62** | | | |
| 204 | $1.49460 \pm 0.00058$ | $0.00780 \pm 0.00058$ | $5.2 \pm 0.6$ |
| 206 | $23.1899 \pm 0.0075$ | $0.0152 \pm 0.0075$ | $6.6 \pm 0.7$ |
| 207 | $22.9223 \pm 0.0086$ | $0.1217 \pm 0.0086$ | $5.3 \pm 0.9$ |
| 208 | $52.393 \pm 0.018$ | $0.115 \pm 0.018$ | $2.2 \pm 1.0$ |
| **Be 96** | | | |
| 204 | $1.41536 \pm 0.00050$ | $0.00189 \pm 0.00050$ | $1.3 \pm 0.6$ |
| 206 | $24.4297 \pm 0.0089$ | $0.0494 \pm 0.0089$ | $2.0 \pm 0.7$ |
| 207 | $22.2584 \pm 0.0093$ | $0.0393 \pm 0.0093$ | $1.8 \pm 0.9$ |
| 208 | $51.897 \pm 0.020$ | $0.009 \pm 0.020$ | $0.2 \pm 1.0$ |

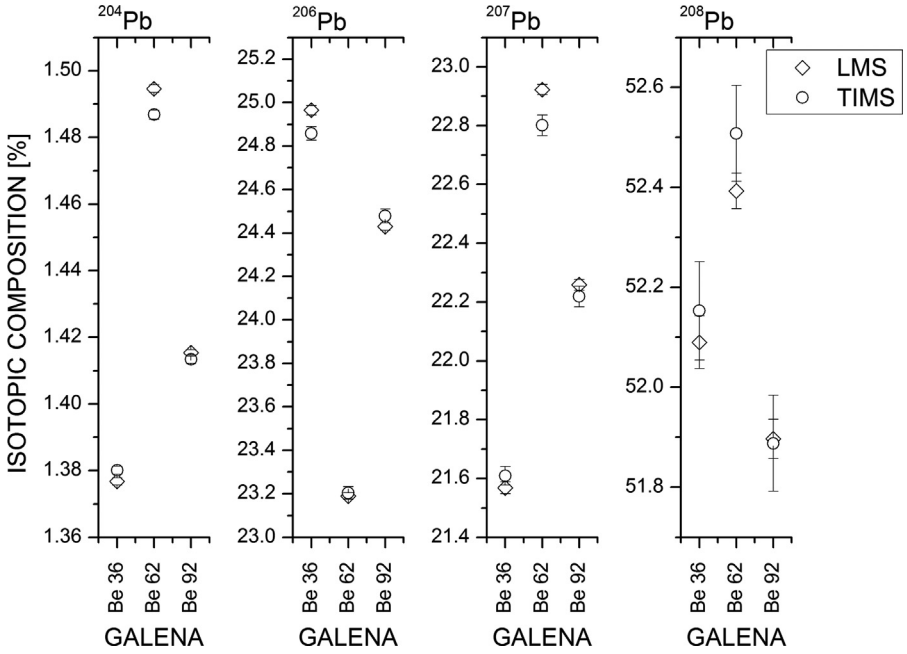


**Fig. 8.** Comparison of Pb isotopic composition measured with TIMS and LMS (Tables 2 and 8). Errors give the 95% confidence level. Best measurement agreement is found for the galena Be 92 campaign.

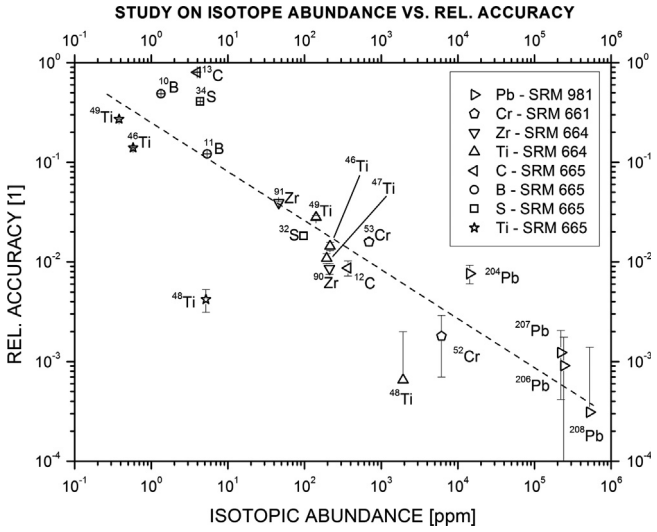


**Fig. 9.** The correlation between the elemental/isotope abundances and relative measurement accuracies. Isotope abundances are given in atomic fraction (from compilation in Table 3).

**Table 9**
Estimate of the accuracy of radio-isotope chronology using $^{207}Pb$–$^{206}Pb$ dating of different grains from a monazite crystal (Sample 449105) investigated by Willigers et al. (2002). Data in the first four columns are taken from Willigers et al. (2002). In the fifth column the uncertainties of the $^{207}Pb/^{206}Pb$ ratio are given by assuming accuracies shown in Fig. 9 (in weight fractions, Table 3). In the last column the corresponding and estimated accuracies are given based on $^{207}Pb/^{206}Pb$ ages given in the fourth column.

| Sample 449105, Grain | $^{206}Pb$ [ppm] | $^{207}Pb$ [ppm] | $^{207}Pb/^{206}Pb$ | $^{207}Pb/^{206}Pb$ age [Myrs] | $^{207}Pb/^{206}Pb$ LMS uncertainty from Fig. 9 [%] | LMS Accuracy [Myrs] |
|---|---|---|---|---|---|---|
| A | 656 | 74 | 0.11261 | $1839 \pm 1$ | 3.5 | $\pm 64$ |
| B | 510 | 57 | 0.11271 | $1838 \pm 1$ | 3.9 | $\pm 71$ |
| B | 667 | 75 | 0.11249 | $1836 \pm 1$ | 3.5 | $\pm 63$ |
| C | 722 | 82 | 0.11328 | $1839 \pm 1$ | 3.4 | $\pm 62$ |
| C | 859 | 97 | 0.11253 | $1836 \pm 1$ | 3.1 | $\pm 56$ |
| D | 517 | 58 | 0.11254 | $1837 \pm 1$ | 3.9 | $\pm 71$ |
| | | | | Stat. accuracy [Myrs] | | $\pm 26$ |

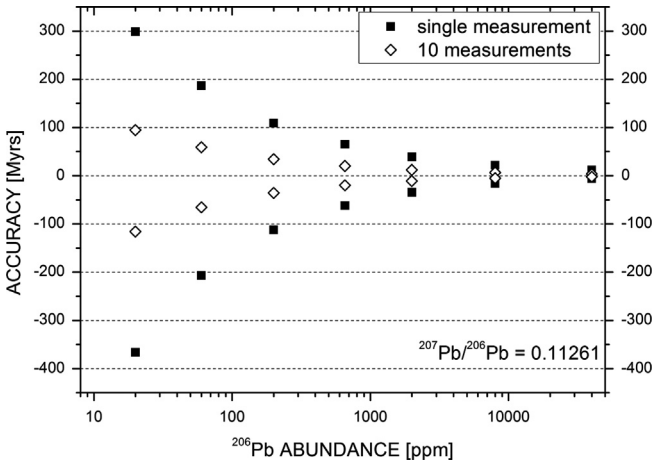


**Fig. 10.** Correlation between $^{207}Pb$ and $^{206}Pb$ abundances and accuracies of $^{207}Pb/^{206}Pb$ dating assuming constant $^{207}Pb/^{206}Pb$ ratio of 0.11261 (Sample 4491105, Grain A, Table 9). Filled squares: estimated age accuracies based on single measurement of one grain. Open diamonds: estimated age accuracies by assuming 10 measurements of different grains, all having the same age.

### 3.4. Measurement accuracy versus laser irradiance

For the quantitative measurement with high accuracy the application of sufficiently high laser irradiance is essential. Most accurate measurements of SRM 981 were conducted by applying a laser irradiance of 0.3 GW/cm$^2$ (see Fig. 6). A similar laser irradiance was used in the investigations of the galena samples. The laser irradiance is a crucial parameter in the ablation process and the efficiency of ion formation for various elements in the plasma is known to differ from one element to another. The laser irradiance primarily affects the ionisation efficiency of the elements. For quantitative studies, the measured elemental abundances thus have to be corrected using calibration factors, the so-called relative sensitivity coefficients (RSC) (Tulej et al., 2011). The quantitative measurements of isotope compositions also show a dependence on the laser irradiance (as shown in the previous sections). It is also expected that the accuracy of the isotope ratios of other elements will be affected by laser irradiance and the optimal laser irradiance can be specific for a particular element. In the following we investigate these dependences by studying the isotopic composition of elements with different concentrations in different NIST standards. The mass spectrometric studies were performed at laser irradiances in the range of 0.5–1.1 GW/cm$^2$. The isotope abundances of several elements were investigated including $^{48}Ti$ ($\sim$1924 ppm, in NIST SRM 664), $^{52}Cr$ ($\sim$525 ppm, NIST SRM 664), $^{90}Zr$ ($\sim$211 ppm, NIST SRM 661), and compared to the Pb case study. Terrestrial isotope ratios were assumed for these elements (Becker, 2007). Mass spectra were obtained by accumulation of 20,000 individual single laser shot spectra from a single sample location.

Fig. 11 displays the dependence of the relative measurement accuracies of $^{48}Ti$ (NIST SRM 664), $^{52}Cr$ (NIST SRM 664), $^{90}Zr$ (NIST SRM 661), and $^{207}Pb$ (NIST SRM 981) on the laser irradiance. A similar dependence of relative accuracies on the laser irradiance is observed as for the Pb study: with increasing laser irradiances a strong improvement in the accuracy is observed, until a stable plateau is reached. At higher laser irradiances the accuracy degrades again. Within a range of about 0.3–0.4 GW/cm$^2$ the measurement accuracy is found to be maximal, at the per mill level.

Each element/isotope has its own optimal irradiance range, defined as the laser irradiance at which the plateau is reached by increasing laser irradiance, at a slightly different laser irradiance, Ti ($\sim$0.70 GW/cm$^2$), Cr ($\sim$0.65 GW/cm$^2$), Zr ($\sim$0.90 GW/cm$^2$), and Pb ($\sim$0.20 GW/cm$^2$). This can be correlated to the boiling temperature of the element (Table 10). Lead with the lowest boiling temperature of 1749 °C has its threshold at the lowest laser irradiance of $\sim$0.20 GW/cm$^2$, whereas Zr with 4406 °C has its threshold at higher irradiance ($\sim$0.90 GW/cm$^2$). Chromium with a slightly lower boiling temperature of 2671 °C than Ti (3287 °C) has its threshold at slightly lower laser irradiance than Ti. Within the plateau of best measurement accuracies a measurement precision of $\sim$2‰ is achieved.

At certain laser irradiances the overall quality of the mass spectra decreases due to saturation of the detector and the electronics, space charge effects in the ion-optical system, and increase of noise. This is observed as a broadening of the mass peaks and a decrease of the dynamic range in the spectra. A decrease of the measurement accuracy can be understood if at least these two effects are modelled. A simulation of relative measurement accuracy by introducing functional description of

$$\text{rel.acc.} \sim \delta/\text{SNR}^{\zeta} \tag{3}$$

$$\text{rel.acc.} \sim \eta(m/\Delta m/\text{SNR})^{\Psi} \tag{4}$$

whereas $\delta$, $\zeta$, $\eta$, and $\Psi$ denote scaling parameters, shows that these effects can significantly change the relative measurement accuracy.

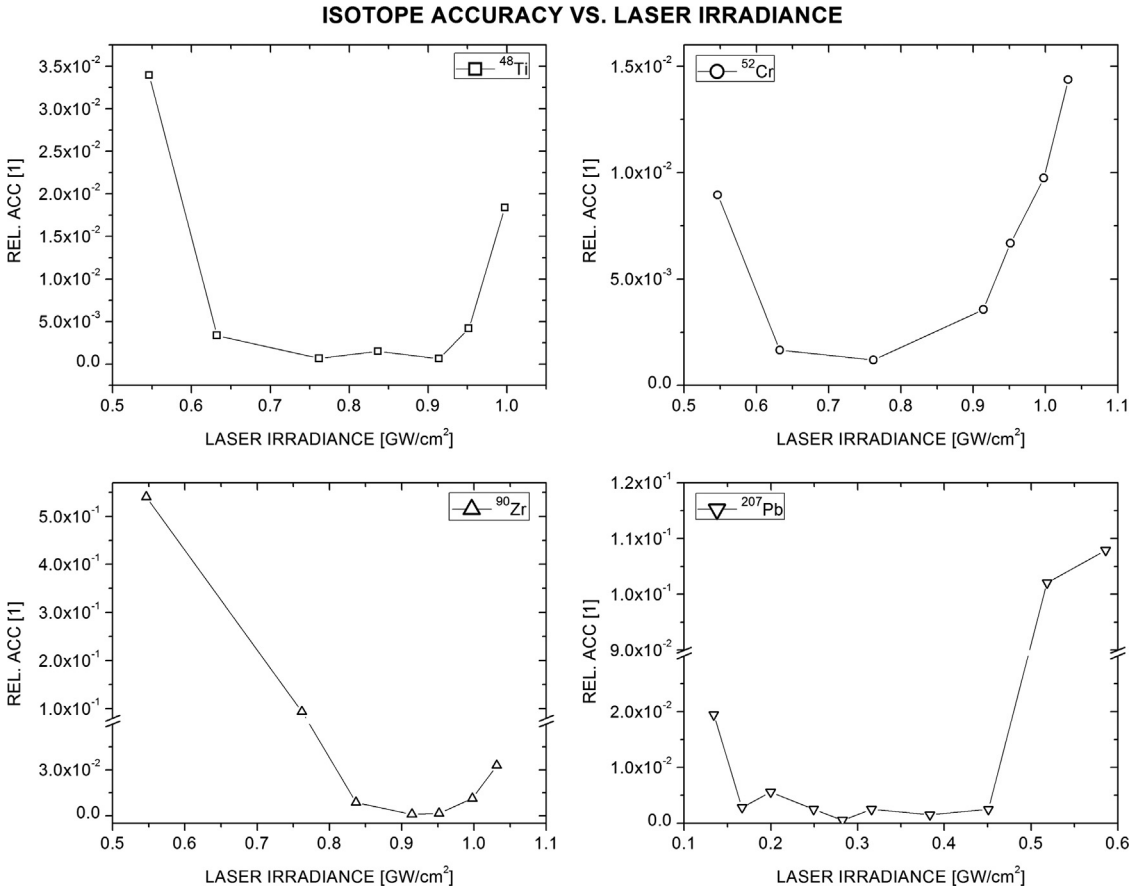


**Fig. 11.** Correlation between relative accuracies of the isotope measurements of $^{48}$Ti, $^{52}$Cr, $^{90}$Zr, $^{207}$Pb and the applied laser irradiance.

**Table 10**
First ionisation potential and boiling temperatures of the elements Ti, Cr, Zr, and Pb (CRC Handbook, 2012).

| Element | First ionisation potential [eV] | Boiling temperature [°C] | Threshold [GW/cm$^2$] |
|---|---|---|---|
| Ti | 6.82812 | 3287 | 0.70 |
| Cr | 6.76651 | 2671 | 0.65 |
| Zr | 6.63390 | 4406 | 0.90 |
| Pb | 7.41663 | 1749 | 0.20 |

Eq. (3), describing the decrease of accuracy at lower laser intensities, models the relation between boiling point of the species and the irradiated laser power. Eq. (4), describing the decrease of accuracy at higher laser powers, models the degradation of the mass spectra for lower mass resolution. Fig. 12 shows these two models together with the relative accuracies in the $^{204}$Pb measurements from Fig. 6, using the parameters $\delta=15$, $\zeta=2$, $\eta=2\times10^8$, and $\Psi=10$.

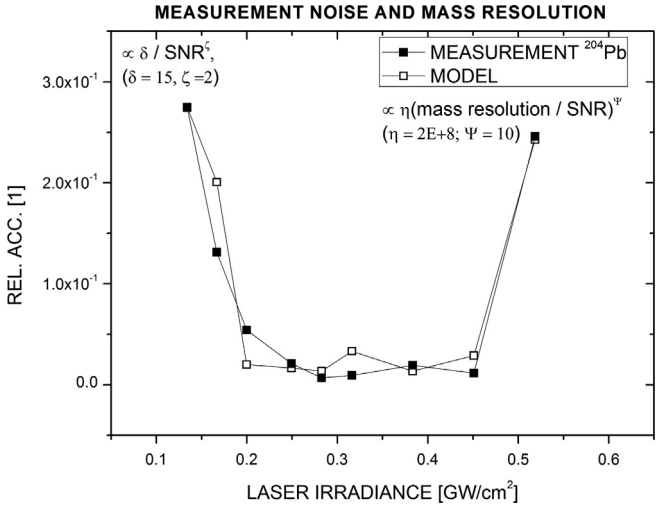


**Fig. 12.** Correlation between relative measurement accuracy of $^{204}$Pb (filled squares) and laser irradiances. Models (1) and (2) (open squares) can explain the dependence of the relative measurement accuracies and the laser irradiance.

## 4. Summary and conclusions

An experimental measurement procedure for precise and accurate measurements of isotope compositions was developed for a miniaturised laser ablation mass spectrometer for space research. The procedure is based on a detailed analysis of laser irradiance, number of accumulated spectra, data analysis method, and optimisation of the instrumental mass resolution $m/\Delta m$ and ion transmission. At optimal experimental conditions measurements of isotope ratios can be conducted within a relative measurement accuracy at the per mill level and better with a precision of ~2‰.

At optimal conditions measurements of Pb isotope compositions in the standard SRM 981 were performed with uncertainties at the level of per mill and better. Measurements of galena samples from different mines show similar relative accuracies and compare well with measurements performed by thermal ionisation mass spectrometry, an established instrument for high level isotopic studies.

Studies of isotope ratios of several other elements in different NIST standards (SRM 661, SRM 664, SRM 665) yielded also relative accuracies and precisions at the per mill level. The laser irradiance and the number of accumulations were found to be the crucial parameters for highly accurate measurements, they are characteristic for each element. A degrading trend of measurement accuracy and precision with lower elemental/isotopic concentration in the sample was observed. Elements/isotopes with concentrations above ~100 ppm can be measured with a relative accuracy and precision at the per mill level. Elements/isotopes with lower abundances have values in the percent range. By the implementation of more sensitive detectors and less noisy acquisition systems more accurate measurements on low abundant isotopes can be expected.

Our investigations show that laser ionisation mass spectrometry can be used for accurate measurements of isotope compositions in solid samples. The precision of this technique is close to that of commonly used techniques that are well accepted in isotope studies, e.g., thermal ionisation mass spectrometry. In situ measurements of isotope patterns are of considerable interest in space research. Our results are encouraging and demonstrate that LMS has the potential for highly accurate in situ isotope ratio measurements of solid materials.

## Acknowledgements

Harry Mischler, Jürg Jost, and Daniele Piazza are acknowledged for their great support in the improvement of the instrument. Thanks to Vera Assis Vernandes for her help in sample preparation and Sylvain Bruderer (Magentasys, Agilent Manufactory Representative) for his support in the data acquisition system. This work is supported by the Swiss National Science Foundation.

## References

Becker, J.S., Dietze, H.J., 2000. Inorganic mass spectrometric methods for trace, ultratrace, isotope, and surface analysis. International Journal of Mass Spectrometry 197, 1–35.

Becker, J.S., 2002. State-of-the-art and progress in precise and accurate isotope ratio measurements by ICP-MS and LA-ICP-MS. Journal of Analytical Atomic Spectrometry 17, 1172–1185.

Becker, J.S., 2005. Inductively coupled plasma mass spectrometry (ICP-MS) and laser ablation ICP-MS for isotope analysis of long-lived radionuclides. International Journal of Mass Spectrometry 242, 183–195.

Becker, J.S., 2007. Inorganic Mass Spectrometry—Principles and Applications. John Wiley & Sons Ltd., England.

Bevington, P.R., Robinson, D.K., 2003. Data Reduction and Error Analysis for the Physical Sciences, third ed. The McGraw-Hill Companies, New York.

Bieler, A., Altwegg, K., Hofer, L., Jäckel, A., Riedo, A., Sémon, T., Wahlström, P., Wurz, P., 2011. Optimization of mass spectrometers using the adaptive particle swarm algorithm. Journal of Mass Spectrometry 46, 1143–1151.

Bieler, A., 2012. Design of a Novel Time of Flight Mass Spectrometer and Practical Application of Computer Optimization to the Development and Tuning of Mass Spectrometers. University of Bern, Switzerland. (Ph.D. thesis).

Blichert-Toft, J., Zanda, B., Ebel, D.S., Albarède, F., 2010. The Solar System primordial lead. Earth and Planetary Science Letters 300, 152–163.

Bouvier, A., Wadhwa, M., 2010. The age of the Solar System redefined by the oldest Pb–Pb age of a meteoritic inclusion. Nature Geoscience 3, 637–641, http://dx.doi.org/10.1038/NGEO941.

Branch, S., Burke, S., Evans, P., Fairman, B., Wolff Briche, C.S.J., 2003. A preliminary study in determining the geographical origin of wheat using isotope ratio inductively coupled plasma mass spectrometry with $^{13}C$, $^{15}N$ mass spectrometry. Journal of Analytical Atomic Spectrometry 18, 17–22.

Brinckerhoff, W.B., Managadze, G.G., McEntire, R.W., Cheng, A.F., Green, W.J., 2000. Laser time-of-flight mass spectrometry for space. Review of Scientific Instruments 71, 536–545.

Cohen, B.A., 2012. Development of the potassium–argon laser experiment (KARLE) instrument for in situ geochronology. In: Proceedings of the 43rd Lunar and Planetary Science Conference, Abstract no. 1267.

CRC Handbook of Chemistry and Physics, 2012. 92nd edition, ⟨http://www.hbcpnetbase.com⟩ (accessed 11.09.12).

Ghazi, A.M., Millette, J.R., 2004. Environmental forensic application of lead isotope ratio determination: a case study using laser ablation sector ICP-MS. Environmental Forensics 5, 97–108.

Gibson, E.K., Pillinger, C.T., Waugh, L.J., 2010. Lunar beagle and lunar astrobiology. Earth, Moon, and Planets 107, 25–42.

Gerstenberger, H., Haase, G., 1997. A highly effective emitter substance for mass spectrometric Pb isotope ratio determinations. Chemical Geology 136, 309–312.

Lin, Y., Yu, Q., Hang, W., Huang, B., 2010. Progress of laser ionization mass spectrometry for elemental analysis—a review of the past decade. Spectrochimica Acta Part B 65, 871–883.

Lobinski, R., Moulin, C., Ortega, R., 2006. Imaging and speciation of trace elements in biological environment. Biochemie 88, 1591–1604.

Managadze, G.G., Shutyaev, I.Y., 1993. Chemical Analysis. 124. Wiley, New York.

Managadze, G.G., Wurz, P., Sagdeev, R.Z., Chumikov, A.E., Tuley, M., Yokovleva, M., Managadze, N.G., Bondarenko, A.L., 2010. Study of the main geochemical characteristics of Phobos' regolith using laser time-of-flight mass spectrometry. Solar System Research 44, 376–384.

McSween Jr., H.Y., Huss, G.R., 2010. Cosmochemistry. Cambridge University Press, Cambridge.

McSween Jr., H.Y., McNutt Jr., R.L., Prettyman, T.H., 2011. Spacecraft instrument technology and cosmochemistry. Proceedings of the National Academy of Sciences 108, 19177–19182.

Nemchin, A.A., Pidgeon, R.T., Whitehouse, M.J., Vaughan, J.P., Meyer, C., 2008. SIMS U–Pb study of zircon from Apollo 14 and 17 breccias: implications for the evolution of lunar KREEP. Geochimica et Cosmochimica Acta 72, 668–689.

Neuland, M.B., Meyer, S., Riedo, A., Tulej, M., Wurz, P., Mezger, K. Probing the allende meteorite with LMS, a miniature laser-ablation mass analyser for space application. Planetary and Space Science. (this issue).

Ng, C.W., Cheung, N.H., 2000. Detection of sodium and potassium in single human red blood cells by 193-nm laser ablative sampling: a feasibility demonstration. Analytical Chemistry 72, 247–250.

Prohaska, T., Köllensperger, G., Hann, S., Stingeder, G., Fitz, W., Wenze, W., 2003. Application of ICP-MS in Environmental Science. In: Holland, G., Tanner, S.D. (Eds.), Plasma source mass spectrometry: applications and emerging technologies. The Royal Society of Chemistry, pp. 93–104.

Pullan, D., Sims, M.R., Wright, I.P., Pillinger, C.T., Trautner, R., 2004. In: Wilson, A. (Ed), Mars Express: The Scientific Payload, ESA SP-1240, 165-204. ESA Publications Division, Noordwijk, Netherlands, ISBN 92-9092-556-6.

Riedo, A., Bieler, A., Neuland, M., Tulej, M., Wurz, P., 2013. Performance evaluation of a miniature laser ablation time-of-flight mass spectrometer designed for in situ investigations in planetary space research. Journal of Mass Spectrometry 48, 1–15.

Rohner, U., Whitby, J.A., Wurz, P., 2003. A miniature laser ablation time-of-flight mass spectrometer for in situ planetary exploration. Measurement Science and Technology 14, 2159–2164.

Rohner, U., Whitby, J., Wurz, P., Barabash, S., 2004. Highly miniaturized laser ablation time-of-flight mass spectrometer for a planetary rover. Review of Scientific Instruments 75, 1314–1322.

Russel, S.S., Hartmann, L., Cuzzi, J., Krot, A.N., Gounelle, M., Weidenschilling, S., 2006. Time scales of the Solar Protoplanetary Disk. In: Lauretta, D.S., McSween, H.Y. (Eds.), Meteorites and the Early Solar Sytem II. The University of Arizona Press, Tucson, Arizona, USA, pp. 233–251.

Russo, R.E., Mao, X., Liu, H., Gonazles, J., Mao, S.S., 2002. Laser ablation in analytical chemistry—a review. Talanta 57, 425–451.

Sinha, M.P., Neidholdt, E.L., Hurowitz, J., Sturhahn, W., Beard, B., Hecht, M.H., 2011. Laser ablation-miniature mass spectrometer for elemental and isotopic analysis of rocks. Review of Scientific Instruments 82, 094102.

Shotyk, W., Zheng, J., Krachler, M., Zdanowicz, C., Koerner, R., Fisher, D., 2005. Predominance of industrial Pb in recent snow (1994–2004) and ice (1842–1996) from Devon Island, Arctic Canada. Geophysical Research Letters 32, L21814.

Todd, J.F.J., Barber, S.J., Wright, I.P., Morgan, G.H., Morse, A.D., Sheridan, S., Leese, M.R., Maynard, J., Evans, S.T., Pillinger, C.T., Drummond, D.L., Heys, S.C., Huq, S.E., Kent, B.J., Sawyer, E.C., Whalley, M.S., Waltham, N.R., 2007. Ion trap mass spectrometry on a comet nucleus: the Ptolemy instrument and the Rosetta space mission. Journal of Mass Spectrometry 42, 1–10.

Tolstikhin, I.N., Kramers, J.D., 2008. The Evolution of Matter. Cambridge University Press, New York.

Tulej, M., Iakovleva, M., Leya, I., Wurz, P., 2011. A miniature mass analyser for in-situ elemental analysis of planetary material–performance studies. Analytical and Bioanalytical Chemistry 399, 2185–2200.

Tulej, M., Riedo, A., Iakovleva, M., Wurz, P., 2012. On applicability of a miniaturised laser ablation time of flight mass spectrometer for trace elements measurements. International Journal of Spectroscopy, 2012, 1–14, (Article ID: 234949), http://dx.doi.org/10.1155/2012/234949.

Willigers, B.J.A., Baker, J.A., Krostad, E.J., Peate, D.W., 2002. Precise and accurate in situ Pb–Pb dating of apatite, monazite, and sphene by laser ablation multiple-collector ICP-MS. Geochimica et Cosmochimica Acta 66, 1051–1066.

Wright, I.P., Barber, S.J., Morgan, G.H., Morse, A.D., Sheridan, S., Andrews, D.J., Maynard, J., Yau, D., Evans, S.T., Leese, M.R., Zarnecki, J.C., Kent, B.J., Waltham, N.R., Whalley, M.S., Heys, S., Drummond, D.L., Edeson, R.L., Sawyer, E.C., Turner, R.F., Pillinger, C.T., 2007. Ptolemy—an instrument to measure stable isotopic ratios of key volatiles on a cometary nucleus. Space Science Reviews 128, 363–381.

Wurz, P., Whitby, J.A., Rohner, U., Martin-Fernandez, J.A., Lammer, H., Kolb, C., 2010. Self-consistent modelling of Mercury's exosphere by sputtering, micro-meteorite impact and photon-stimulated desorption. Planetary and Space Science 58, 1599–1616. (Corrigendum Planetary and Space Science 2010, 58, p. 2051).

Yu, Q., Huang, R., Hang, W., He, J., Huang, B., 2009a. Laser ionization time-of-flight mass spectrometry for direct elemental analysis. Trends in Analytical Chemistry 28, 1174–1185.

Yu, Q., Cao, Z., Li, L., Yan, B., Hang, W., He, J., Huang, B., 2009b. Applicability of standardless semiquantitative analysis of solids by high-irradiance laser ionization orthogonal time-of-fight mass spectrometry. Analytical Chemistry 81, 4343–4348.
Zhang, B., He, M., Hang, W., Huang, B., 2013. Minimizing matrix effect by femtosecond laser ablation and ionization in elemental determination. Analytical Chemistry 85, 4507–4511.
Zoriy, M.V., Dehnhardt, M., Reifenberger, G., Zilles, K., Becker, J.S., 2006. Imaging of Cu, Zn, Pb and U in human brain tumor resections by laser ablation inductively coupled plasma mass spectrometry. International Journal of Mass Spectrometry 257, 27–33.